



Cite this: *Analyst*, 2024, **149**, 2122

Label-free mapping of cetuximab in multi-layered tumor oral mucosa models by atomic force-microscopy-based infrared spectroscopy†

Gregor Germer, ^{‡a} Leonie Schwartz, ^{‡b} Jill García-Miller, ^b
 Roberta Balansin-Rigon, ^{b,c} Lucie J. Groth, ^a Isabel Rühl, ^a Piotr Patoka, ^a
 Christian Zoschke ^{*b,d} and Eckart Rühl ^{*a}

Sensitive mapping of drugs and drug delivery systems is pivotal for the understanding and improvement of treatment options. Since labeling alters the physicochemical and potentially the pharmacological properties of the molecule of interest, its label-free detection by photothermal expansion is investigated. We report on a proof-of-concept study to map the cetuximab distribution by atomic-force microscopy-based infrared spectroscopy (AFM-IR). The monoclonal antibody cetuximab was applied to a human tumor oral mucosa model, consisting of a tumor epithelium on a lamina propria equivalent. Hyperspectral imaging in the wavenumber regime between 903 cm⁻¹ and 1312 cm⁻¹ and a probing distance between the data points down to 10 × 10 nm are used for determining the local drug distribution. The local distinction of cetuximab from the tissue background is gained by linear combination modeling making use of reference spectra of the drug and untreated models. The results from this approach are compared to principal component analyses, yielding comparable results. Even single molecule detection appears feasible. The results indicate that cetuximab penetrates the cytosol of tumor cells but does not bind to structures in the cell membrane. In conclusion, AFM-IR mapping of cetuximab proved to sensitively determine drug concentrations at an unprecedented spatial resolution without the need for drug labeling.

Received 29th October 2023,
 Accepted 20th February 2024
 DOI: 10.1039/d3an01877f

rsc.li/analyst

Introduction

Anti-tumor therapy has been revolutionized with a multitude of selective monoclonal antibodies, which flag cancer cells, block immune system inhibitors, or downregulate cell growth.¹ Despite these major therapeutic improvements, cancer still remains one of the most frequent causes of death. The survival rates of patients with advanced melanoma or with head and neck cancers stagnate at about 60%.² The prognosis remains even worse for patients with locally advanced tumors or distant metastatic disease at the time of initial diagnosis.

Recently, we developed multi-layered tumor oral mucosa (TOM) models for studying drug uptake, distribution and

efficacy as well as drug resistance mechanisms.^{3,4} The TOM models recapitulate the morphology, grading, and protein expression profiles of patient tumors. Moreover, the application of two drugs from clinical routine treatment (docetaxel and cetuximab) resulted in similar effects compared to the patients' tumors. Fluorescence lifetime imaging microscopy (FLIM) revealed the interactions between cetuximab and cells, yet the efficacy of cetuximab was limited in both models and patients.³

Fluorescent labels are most commonly used to detect the molecule of interest in biological specimens. In addition to the availability, fluorescence microscopy reaches the limit of single molecule detection.⁵ Analyzing the fluorescence lifetime (FLIM) provides insights into the physicochemical microenvironments of the label.⁶ The diffraction limited spatial resolution of FLIM often impedes subcellular analyses, but superresolution techniques can overcome this limitation.⁷

Nevertheless, labeling might alter the physicochemical and pharmacological properties of drugs, which motivates the use of label-free spectromicroscopy techniques in this work. Label-free methods include mass spectrometry imaging,⁸ optical coherence tomography,⁹ scanning transmission X-ray microscopy,^{10,11} spontaneous as well as stimulated Raman scattering (SRS),^{12–14} scattering optical near-field microscopy (s-SNOM),^{15,16} and atomic force microscopy-based infrared-

^aPhysical Chemistry, Freie Universität Berlin, Arnimallee 22, 14195 Berlin, Germany. E-mail: ruehl@zedat.fu-berlin.de

^bInstitute of Pharmacy, Freie Universität Berlin, Königin-Luise Str. 2+4, 14195 Berlin, Germany. E-mail: christian.zoschke@fu-berlin.de

^cSchool of Pharmaceutical Sciences, University of Campinas, R. Candido Portinari, 200 – Cidade Universitária, Campinas, SP, 13083-871, Brazil

^dDepartment of Veterinary Medicines, Federal Office of Consumer Protection and Food Safety, Gerichtstr. 49, 13347 Berlin, Germany

†Electronic supplementary information (ESI) available. See DOI: <https://doi.org/10.1039/d3an01877f>

*Contributed equally/shared 1st authorship.



spectroscopy (AFM-IR).¹⁷ The sensitivity of this technique was enhanced by using metalized tips so that even self-assembled monolayers could be investigated.¹⁸ AFM-IR has shown to be widely used for various applications. Specifically, high chemical selectivity along with spatial resolution on the nanoscale, *i.e.*, far below the diffraction limit of optical microscopy, is helpful to identify mechanisms of drug uptake and drug-target interactions.¹⁹

In the present study, we investigate the cetuximab uptake and distribution into TOM models. We assessed whether this monoclonal antibody could be selectively traced within the TOM models. Furthermore, we compared cetuximab amounts within the tumor mass following two different routes of drug administration, topically to the mucosa surface or systemically to the culture medium. Finally, we mapped the cetuximab distribution on a cellular level to delineate possible resistance mechanisms.

Experimental

Spectromicroscopy experiments were carried out using a nano-IR2-s instrument (Anasys, Anaheim, CA, U.S.A./Bruker, Karlsruhe, Germany), which contains an atomic force microscope and a tunable infrared laser source.¹⁹ It was operated in the photothermal expansion mode (AFM-IR),¹⁷ which made use of pulsed infrared laser radiation from a tunable quantum cascade laser (MIRcat-QTTM, DRS Daylight Solutions, U.S.A.) in the resonance-enhanced contact mode. Tunable radiation in the range of 903–1312 cm⁻¹ was focused onto the sample in the proximity of the tip of the atomic force microscopy (AFM). This allows for topography measurements as well as local chemical analysis of the samples at ambient conditions. This leads to local absorption spectra, which were taken in the hyperspectral imaging mode. This results in infrared spectra with a probing distance between the data points reaching down to 10 × 10 nm.

Cetuximab (molecular weight: 146 kDa) was purchased from Selleckchem (Houston, TX, U.S.A.). Human oral keratinocytes and fibroblasts, as well as their culture media, were purchased from ScienCell (Carlsbad, CA, U.S.A.). The head and neck squamous cell carcinoma cell line SCC-25 (RRID: CVCL_1682)²⁰ was a generous gift from Howard Green, Dana-Farber Cancer Institute; Boston, MA, U.S.A. Collagen-G, DMEM 10×, fetal calf serum, and HEPES buffer were purchased from Biochrom (Darmstadt, Germany). The 12-well plates and 12-well inserts (0.4 μm pore size) for model building were obtained from Greiner bio-one (Leipzig, Germany). The model medium components adenine HCl monohydrate, amphotericin B, cholera toxin, DMEM, DMEM/F-12 GlutaMAX, hydrocortisone, insulin, L-ascorbic acid, penicillin-streptomycin-solution (pen/strep), transferrin, and triiodo-L-thyronine, were purchased from Sigma Aldrich (Munich, Germany). Epidermal growth factor and non-essential amino acids were purchased from Thermo Fisher Scientific (Waltham, MA, U.S.A.).

Cell cultures were prepared as follows: human oral keratinocytes and fibroblasts were cultured in an oral keratinocyte and

fibroblast medium, respectively. The SCC-25 cell line was grown in DMEM/F-12 Ham medium, supplemented with 9% fetal calf serum, 0.9% L-glutamine, and penicillin/streptomycin. The cell line was regularly checked by single nucleotide polymorphism authentication (Multiplexion, Heidelberg, Germany). The cells were incubated at 37 °C in a humidified atmosphere containing 5% CO₂. The medium was changed three times a week, and the cells were passaged after reaching confluency of 80%. Cell cultures were performed according to standard operating procedures and referred to good cell culture practice. The TOM models were built and treated as described earlier.³ Briefly, human oral fibroblasts (0.1 × 10⁶ cells per well) were embedded into a collagen-based compartment for each model, resembling the lamina propria. After one week, the upper epithelial layer was built out of 80% human oral keratinocytes (0.8 × 10⁶ cells per well), co-cultured with 20% of SCC-25 tumor cells. In the first two weeks, the models were cultured and submerged with the construct growth medium. The medium was changed to construct the differentiation medium in the third and last week of cultivation, by keeping the models surface medium-free to expose the epithelium to ambient air. The model medium was changed three times a week and models were incubated at 37 °C in a humidified atmosphere with 5% CO₂. Cetuximab was solubilized in PBS to prepare a stock solution of 5.2 mg mL⁻¹ and diluted with the model medium to 100 μg mL⁻¹ yielding a resulting concentration of 0.2% PBS. Cetuximab treatment started one day after tumor cell seeding and was applied in total five times in a 48 h rhythm, considering the doubling time of about 50 h for SCC-25 cells.³ The drug was put on top of the model, corresponding to a topical application of 40 μL. The solvent control model was treated with 0.2% PBS instead of cetuximab. After a total incubation time of 3 weeks, the models were snap-frozen and cut into 1 μm thick pieces on 5 × 5 mm silicon substrates for AFM-IR analysis. The samples were slowly dried at -19 °C before use and were investigated at ambient conditions, which leads to defects in the investigated samples (*cf.* Fig. 1).

The AFM-IR studies on TOM models used a 450 μm long gold-coated silicon AFM tip with a nominal radius of 25 nm (Bruker, model: PR-EX-nIR2-10, resonance frequency of 13 ± 4 kHz, spring constant: 0.07–0.4 N m⁻¹). AFM-IR spectra were acquired at a sweep speed of 100 cm⁻¹ s⁻¹ and a spectral point density of 1 cm⁻¹ was used. The average of the infrared laser power applied to the sample was of the order of 1.5 mW. The repetition rate of the pulsed laser radiation was adjusted in the range of 150 kHz to 220 kHz depending on the contact resonance frequency that might change during the measurements. The laser power spectrum and the AFM-IR amplitudes were normalized to the emitted laser power, which varied as a function of the incident wavelength. The hyperspectral imaging infrared maps were recorded with a pixel size of 40 × 40 nm at low spatial resolution and 10 × 10 nm at high spatial resolution, respectively. The pixel size corresponds to the distance between the data acquisition points, whereas the spatial resolution in the scan direction depends on the size of the AFM-tip and is estimated to be ~25 nm. The vertical resolution depends on the penetration of the incident infrared radiation



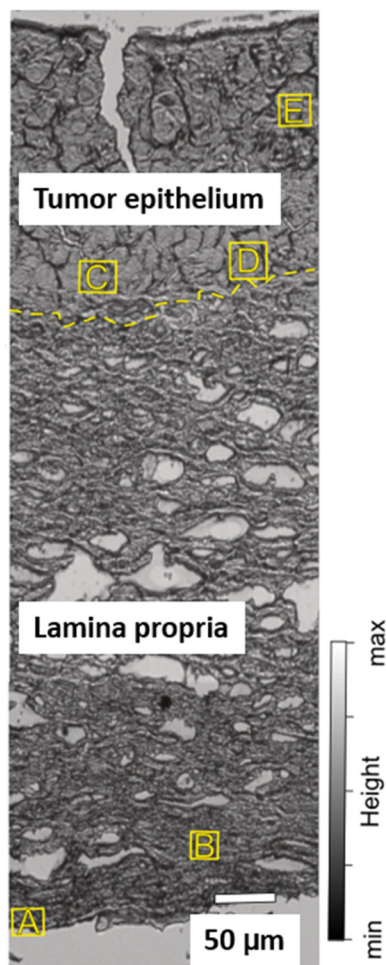


Fig. 1 Optical micrograph of topically treated TOM models with the SCC-25 cells denoted as tumor epithelium (top) and the collagen denoted as lamina propria (bottom). The yellow dashed line marks the interface between epithelial layer and the lamina propria. The sample shows defects occurring after topical treatment due to defrosting, drying, and cutting. Investigated regions are marked by yellow squares labeled A–E.

and the thickness of the samples that is kept below 1 μm . This small sample thickness is of importance for the spatial resolution, as thick samples gather a photothermal expansion response from a larger area, while the infrared radiation will penetrate the entire sample and reaches the substrate. Any distortions of the AFM-IR signal due to molecular orientation are unlikely to occur, as the molecules are expected to be randomly oriented in the biological matrix. As the response of the silicon substrate can be probed, we assume that entire sample thickness can contribute to the AFM-IR response.

Results and discussion

The AFM-IR images depict the morphology of the TOM model with the collagen containing lamina propria (Fig. 1, bottom) and the cancerous tumor epithelium (Fig. 1, top).³ The cetuxi-

mab solution was added either to the culture medium underneath the lamina propria or onto the TOM model surface, corresponding to systemic or topical treatment, respectively. Regions of interest were selected for AFM-IR studies, marked by yellow squares A to E (Fig. 1). Untreated TOM models were investigated as reference samples for comparison (ESI, Fig. S1†).

AFM-IR relies, as other label-free spectromicroscopy methods, on reference spectra of the contained species taken by the same experimental approach. AFM-IR spectra were obtained from a dried drop-coated solution of cetuximab in PBS on a silicon substrate (Fig. 2(a)) and two different regions of an untreated TOM model (Fig. 2(b), and (c)). These reference spectra were used to determine the local variability in AFM-IR spectra. The spectrum taken at the lamina propria shows slight differences in local absorption, which are assumed to be due to natural variability and different cellular contributions of the spatially resolved spectra (Fig. 2(d) and (e)). Further, reference spectra of PBS (Fig. 2(f)), the PEG-based cryo medium (Fig. 2(g)), and the silicon substrate (Fig. 2(h)) were taken, respectively.

The most intense spectral features in the AFM-IR spectrum of cetuximab are found at 1223 cm^{-1} (spectral assignment: histidine, $\delta(\text{CH})$, $\nu(\text{C-N})$, $\delta(\text{NH})$) and 1274 cm^{-1} (spectral assignment: tyrosine-OH $\nu(\text{C-O})$), respectively.^{21,22} Both prominent bands contribute to a unique shape of cetuximab compared to the other reference AFM-IR spectra, whereas any histidine and

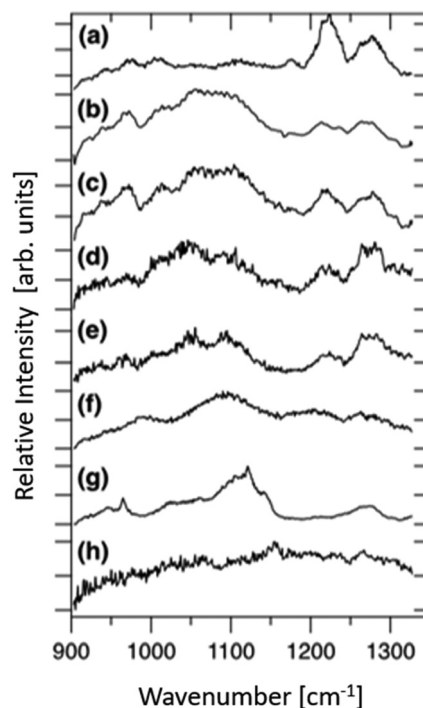


Fig. 2 AFM-IR reference spectra of (a) cetuximab on a silicon substrate; (b) reference tumor cell 1; (c) reference tumor cell 2; (d) lamina propria location 1, (e) lamina propria location 2, (f) PBS; (g) PEG-based cryo medium; (h) silicon substrate. These reference spectra were used as input for the linear combination modeling-based analysis for determining the local cetuximab distribution at separate locations (cf. Fig. 1) of the topically treated TOM model (see Fig. 4, top row).



tyrosine contained in the biological matrix is contained in the weak background signal in this spectral regime (*cf.* Fig. 2(b) and (c)). There is, however, also absorption of the other reference compounds in the same wavenumber regime (Fig. 2). Specifically, this is the case for the vehicle control TOM model at two locations, indicated by reference tumor cell 1 and 2 (Fig. 2(b) and (c)), but with a different intensity distribution compared to cetuximab. These reference spectra were used to derive an average AFM-IR spectrum that is used for data reduction (see below). The intensity ratio of the bands occurring between 1200–1300 cm⁻¹ of the lamina propria (Fig. 2(d) and (e)) is distinctly different from that of cetuximab. The remaining AFM-IR reference spectra taken of PBS, the PEG-based cryo medium, and the silicon substrate do not show distinct spectral features in the regions where cetuximab absorbs (Fig. 2(f)–(h)).

The AFM-IR spectra are evaluated with respect to their local composition using a linear combination modeling approach,^{11,23–26} which is based on recent developments used for the analysis of stacks of soft X-ray micrographs recorded by scanning transmission X-ray microscopy.¹¹ Briefly, weight factors of the individual components represented by reference spectra were obtained from a script written in Igor Pro 9 (WaveMetrics, Lake Oswego, OR, U.S.A.) using a Levenberg-Marquardt algorithm. This minimizes the deviations of the weighted sum of the reference spectra from the experimental AFM-IR spectrum contained in each pixel.²⁷

$$\text{Spectrum}(E) = \sum_i a_i \cdot \text{Reference Spectrum}_i(E) + n. \quad (1)$$

Eqn (1) indicates that the experimental AFM-IR spectrum of each pixel of the spectromicrographs as a function of photon energy E (expressed in cm⁻¹ and denoted as $\text{Spectrum}(E)$) is described by the sum of the reference spectra ($\text{Reference Spectrum}(E)$) of the contained species with a given local abundance a_i . The exact composition of the sample at a given location is unknown. Therefore, only the most abundant species have been considered in this analysis, such as contributions from untreated TOM models, lamina propria (collagen), PBS, the cryo medium, cetuximab, and the silicon substrate. Furthermore, a background contribution is also included by the constant n . The derived weight factors represent the local concentrations of the major components in the samples. This is sufficient since it is primarily aimed to probe label-free the local distribution of cetuximab in the biological matrix ($a_{\text{cetuximab}}$).

Alternatively, a reference spectra-based principal component analysis (PCA) of a hyperspectral measurement of a reference tumor cell was performed, as derived from a numerical non-negative matrix factorization of the average AFM-IR spectrum.^{28,29} Igor Pro offers a PCA algorithm, where the component 1 corresponds almost to the average spectrum of the investigated region, the other components represent difference spectra relative to the average, *i.e.*, they may contain positive and negative contributions (see Fig. 3). In principle, the PCA components may correspond to real constituents, but in most

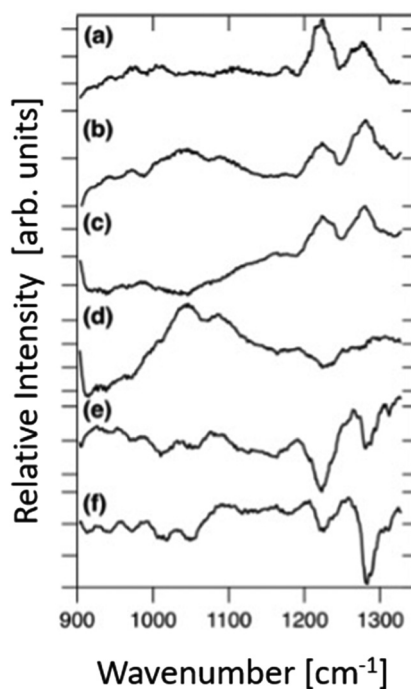


Fig. 3 (a) AFM-IR reference spectrum of cetuximab on a silicon substrate. Results from a principal component analysis of a reference tumor cell within the epithelium: (b) component 1; (c) component 2; (d) component 3; (e) component 4; (f) component 5. These spectra were used as input for the principal component-based analysis for determining the local cetuximab distribution at separate locations (*cf.* Fig. 1) of the topically treated TOM model (see Fig. 4, bottom row).

cases these are probably due to a superposition of several species contained in the biological sample.^{30,31} In the singular value decomposition-based PCA analysis the data matrix decomposition is built on an orthogonal set of dominant factors, such as eigenvectors, which might not have any physical meaning. This analysis provides only a linear combination to fulfill the orthogonal constraints.³¹ The result of this approach is shown for the first five principal components in Fig. 3(b)–(f) besides the AFM-IR spectrum of cetuximab (see Fig. 3(a)). These components represent the natural local variability of the biological system. The first component is shown in Fig. 3(b). It is similar in shape to the vehicle control, *i.e.*, the AFM-IR spectrum of the topically TOM model (*cf.* Fig. 2(b) and (c)). Contributions of further weak components was tried (not shown), but these were verified to have no influence on the data analysis. The eigenvectors of each component were scaled to have a contribution of at least 0.5% to the total intensity in each pixel, which corresponds to the sum of all eigenvector lengths.

The lower limit for the derived weight factors the substance spectra shown in Fig. 3(a) and (b) was set to zero, as required for a non-negative matrix factorization. No limits were used for the other components shown in Fig. 3(c)–(f). This approach has the advantage, as compared to a classical singular value decomposition, that negative values for the substance-specific components substances are avoided, while the spectral vari-



ations due to the heterogeneity of the biological matrix can be represented by the other components. This approach allows us to combine the advantages of numerical singular value decomposition and non-negative matrix factorization to be included in this analysis, which also relies on the Levenberg–Marquardt algorithm written in Igor Pro 9. Small spectral shifts were also considered in this analysis, which might arise from different surroundings of the absorbers, but these did not influence the results of the local drug distributions observed in the lamina propria and the tumor cells and are therefore not shown.

Fig. 4 shows the results of local label-free probing of cetuximab at the arbitrarily selected locations, as indicated in Fig. 1. The spatially resolved local concentrations of cetuximab ($a_{\text{cetuximab}}$) are based on the evaluations on reference spectra (see Fig. 2) and principal component analysis (see Fig. 3 for the tumor cell region and in the ESI, Fig. S6† for the lamina propria), respectively. These results are shown in Fig. 4 in the top (for linear combination modeling: A1, B1, C1, D1, and E1) and the bottom row (for principal component analysis: A2, B2, C2, D2, and E2), respectively. The minimum value of the abundance of cetuximab ($a_{\text{cetuximab}}$) was set to 0.2, which follows from experiments on the untreated TOM model. This value is derived from the vehicle control reference sample, as shown in the ESI (see Fig. S1 and S2†). There are no detectable spectral shifts of the drug compared to the cellular background on which the drug is superimposed, reaching down to single molecule detection, as is outlined further below. Furthermore, we have analyzed the spatial distributions of the other species and principal components at three selected locations for the

untreated reference sample (ESI, Fig. S3–S5†), the topically treated sample at five locations (ESI, Fig. S7–S11†), and a systemically treated sample that was drug-exposed from the collagen (lamina propria) side and analyzed at four locations (cf. ESI, Fig. S12–S16†).

The local concentration of cetuximab is color-coded according to these analyses, where a background signal of 0.20 ± 0.03 corresponds to the quantification limit, as is determined from untreated reference tumor cells in the wavenumber regime from 1190 cm^{-1} to 1320 cm^{-1} due to cross sensitivities of the tumor cells (see ESI, Fig. S1 and S2†). The detection limit is slightly different for the lamina propria, where a value of 0.17 ± 0.03 is determined, the quantification limit is found at 0.35 ± 0.03 . The spatial distributions of cetuximab are superimposed to AFM images for correlating the properties of the biological matrix and cell morphology with local drug distributions. Both analysis approaches yield comparable results: the drug can be determined at all selected cells and depth levels after 10 days of topical treatment (Fig. 1). Similar findings were obtained from a “systemic treatment” where the drug was applied to the model medium (see ESI, Fig. S12–S16†). There, a somewhat higher abundance of cetuximab was observed, as follows from a comparison of the color scales of Fig. 4 and S12.† Thus, topical administration of cetuximab might be a promising option for the oral cancer treatment with reduced systemic side effects.³² Furthermore, the spatial distribution of cetuximab mapped by AFM-IR within the TOM model matches the distribution of the drug as derived from FLIM,³ *i.e.*, there is general agreement between label-based and label-free spectromicroscopy, which further corroborates

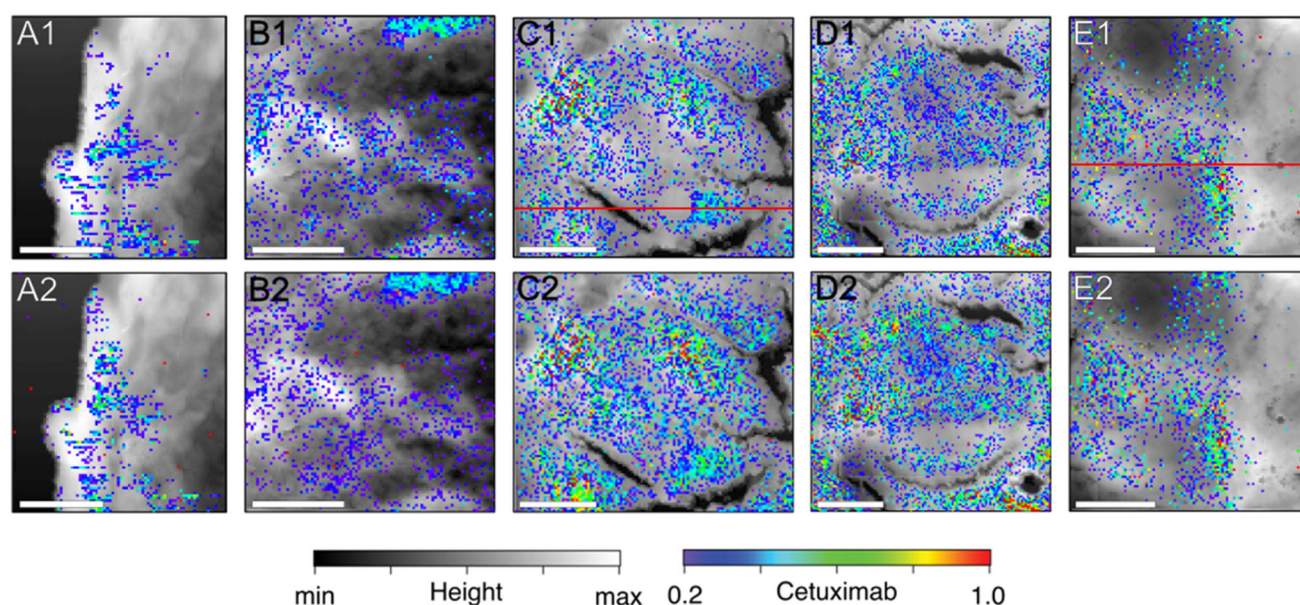


Fig. 4 Local cetuximab distribution at regions in the lamina propria (A and B) and in the tumor epithelium (C–E). Top row: Relative local cetuximab distribution using linear combination modeling of reference spectra (cf. Fig. 2). Bottom row: Relative local cetuximab distribution obtained from a singular value decomposition-based PCA analysis (cf. Fig. 3 and Fig. S6†). The color code represents the relative local cetuximab abundance. The horizontal red lines in C1 and E1 correspond to cuts in local cetuximab concentration shown in Fig. 5. Scale bar: 10 μm . See text for further details.



the present results that do not require labeling of the drug for sensitive probing. In addition, AFM-IR not only confirms the drug distribution patterns in regions of high drug concentration, but also probes low amounts of cetuximab in the lamina propria. Further advantages of label-free probing of cetuximab in TOM models are discussed below along with high spatial resolution and single molecule detection that is not possible to reach by FLIM.

Simple changes in optical density cannot be used for determining the local cetuximab distribution in the samples under study due to the similarity in spectral shape of the biological matrix and cetuximab, which underscores the need for the applied analysis approaches. Specifically, in linear combination modeling the entire shapes of the reference spectra are of importance for identifying cetuximab. Its distribution is superimposed to a background signal of the biological matrix of untreated cells (*cf.* Fig. S2†), as pointed out above. In the principal component analysis, all major components shown in Fig. 3 including the spectrum of the drug were used for deriving *via* a singular value decomposition the local cetuximab distribution, which is remarkably similar to that obtained from linear combination modeling using reference spectra of the major components (*cf.* Fig. 2). Fig. 4(C2–E2) shows the drug distribution based on the reference set of a principal component analysis, whereas the drug distribution in the lamina propria (Fig. 4(A2 and B2)) was derived from a different set of principal components depicted in the ESI, Fig. S6† and is almost identical to that derived from reference spectra (Fig. 4(A1 and B1)). This indicates the general consistency and robustness of the data analysis with respect to the identification of cetuximab and its spatial distribution.

The AFM-IR approach is in general bulk sensitive where the probed volume is located below the AFM tip and can reach the silicon substrate in $\sim 1\ \mu\text{m}$ depth. This is unlike scattering optical near-field microscopy (s-SNOM), which is a more surface sensitive approach.^{33–36} Since the entire sample volume below the AFM-tip contributes to the AFM-IR signal, the drug can be located inside the cells, or is sticking on cell membranes. Almost no drug is found near the cross-sections of the cell membranes, which are characterized by narrow dark regions in Fig. 4. Small amounts of cetuximab are found in the cytosol of tumor cells in the TOM models. The granular appearance and the size of the cetuximab signals hint to an internalization of cetuximab *via* endocytosis, similar to recent work.³⁷ However, the absence of cetuximab at the cell membrane and the low intracellular concentration correspond to the limited efficacy of cetuximab in reducing the tumor size (*cf.* Fig. 1 and Fig. S1†).³² To reduce the tumor size, cetuximab needs to bind the cytoplasmic domain of the epidermal growth factor.³⁸ Rhodamine labeled cetuximab was used in earlier studies to probe the location of this monoclonal antibody upon uptake by clathrin-mediated endocytosis into A431, A549 or HCT-116 cells.³⁹ Evidently, the data analysis using linear combination modeling of reference spectra yields more distinct results than the principal component analysis shown

in Fig. 4(C2–E2), as is evident from the less clear nuclear region containing no cetuximab.

Next, we determined the local cetuximab intensity within arbitrarily selected regions (red lines in Fig. 4 at the locations C1 and E1). The drug intensity only occurs with discrete steps in amplitude, where the scales used in Fig. 4 and 5 were kept identical. Note that some negative intensity occurs in Fig. 5(b) due to data reduction. It is assumed that the smallest step height corresponds to absorption of a single cetuximab moiety. Then, one can establish a vertical scale of the probed cetuximab molecules at a given location, indicating that up to eight individual molecules are probed in each pixel (Fig. 5). Note that this drug distribution is not correlated with the local height or thickness of the sample, which appears to be rather flat in most regions. Therefore, we assume that only absorbing drug molecules correspond to the signal shown in Fig. 5(a) and (b). Such discrete steps in amplitude are not expected to be found for low molecular weight drugs, but due to the substantial molecular weight of cetuximab (146 kDa) and its substantial diameter probed in the volume of $40 \times 40\ \text{nm} \times 1000\ \text{nm}$, corresponding to $1.6 \times 10^{-3}\ \mu\text{m}^3$, even single molecule detection appears possible in this sensitive label-free approach. This result is in general agreement with recent work using related techniques that even allowed for the determination of the secondary structure of proteins.^{40,41} The difference to these works is that the drug is not deposited on a substrate rather than it is embedded in a biological matrix.

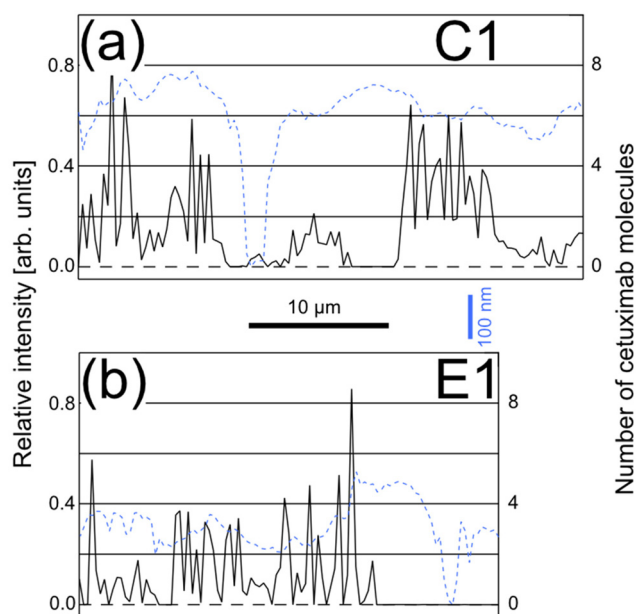


Fig. 5 Intensity of the relative cetuximab concentration shown in Fig. 4: (a) location C1 and (b) location E1, as indicated in Fig. 4 by red lines. The scale on the right-hand side comes from a tentative assignment of the amplitude of the cetuximab signal in terms of single molecule detection (scale bar: $10\ \mu\text{m}$). The blue dashed traces in (a) and (b) correspond to the height scans using the AFM (the vertical scale bar is indicated by blue color). See text for further details.



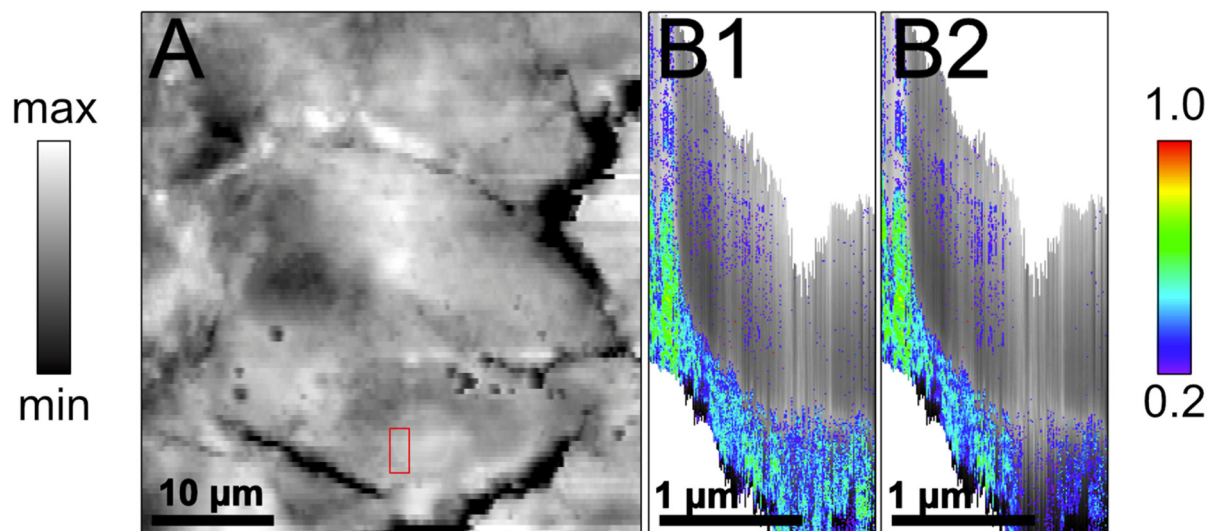


Fig. 6 High-resolution scans of cetuximab in the tumor cell cytosol. The scanned region is marked by the red rectangle in the AFM image (A) recorded at location C of Fig. 1 in the topically treated TOM model. Height distribution in grey; the color code represents the relative local cetuximab abundance. Pixel size: 10×10 nm. B1: cetuximab distribution based on linear combination modeling of reference spectra (*cf.* Fig. 2 and 4); B2: cetuximab distribution based on a singular value decomposition-based PCA analysis (*cf.* Fig. 3 and 4).

The location of the cell nucleus at location C (*cf.* Fig. 1) is investigated with smaller pixel sizes of 10×10 nm for verifying the results obtained from Fig. 4. The selected location is marked by a red rectangle in Fig. 6(A), where the height distribution of this cell region is shown. Clearly visible is an almost annular structure of 5.2 ± 0.4 μm diameter and an apparent thickness of ~ 400 nm, that is assigned to a cut through the nuclear membrane. However, the height-based contrast by atomic force microscopy does not resolve all nuclear envelope substructures.⁴² At this small pixel size, the stability of the instrument reaches its limits, leading to lateral drifts during data acquisition, which were corrected manually after data collection. Both analysis approaches, *i.e.*, linear combination modeling (Fig. 6(B1)) and singular value decomposition-based PCA analysis (Fig. 6(B2)), show a distinct drop in cetuximab concentration at the nuclear membrane to cetuximab concentrations below the limit of detection inside the nucleus, where the spurious signal inside the nucleus is assigned to cross sensitivities near the detection limit (*cf.* ESI†).

This assignment is supported by additional investigations of control samples, in which no such steep concentration gradient is observed near nuclei (see ESI, Fig. S1 and S2(B1), (B2)†). In addition, the spatial distributions of other analyzed species and principal components also show no resemblance to that of cetuximab, as shown in the ESI, Fig. S17.† The local drug concentration around the nuclear membrane appears to be even at high spatial resolution fairly homogeneous, despite some artefacts caused by the line-wise scans in vertical direction. Finally, it is noted that the spatial distributions of cetuximab are in agreement with recent work employing fluorescence lifetime imaging (FLIM) on the same tumor model.³ This implies that both label-free spectromicroscopy and fluorescence-based labels provide similar results. The advantage of

the present approach is that no labels are required that might change the efficacy of the drug and the spatial resolution is significantly higher than in FLIM.

The specific advantage of the label-free detection by AFM-IR and associated data evaluation is that this approach is not limited to a specific drug or a given spectral regime and can be widely applied without modification of the drug or drug delivery system by a specific label. Further progress with respect to accelerated data acquisition is anticipated, by making use of a reduced number of measurements along with mathematical approaches, such as compressed sensing or low-rank matrix evaluations.^{43–45} Such approaches reduce the data acquisition times of high-spatial resolution scans by an order of magnitude without losing neither spatial resolution nor chemical selectivity. Then, lateral drifts can be reduced and further details of drug localization reaching the molecular scale can be discovered, which is currently not possible. This goes, however, beyond the scope of this work and requires further instrumental developments.

Summary and conclusions

AFM-IR sensitively probes in a label-free approach cetuximab within a multitude of other substances contained in a multi-layered tumor oral mucosa (TOM) model. Crucial for such label-free probing is the data analysis by linear combination modeling of reference spectra as well as singular value decomposition-based PCA analysis. Besides high spatial resolution with pixel sizes down to 10×10 nm, single molecular detection of high-molecular weight substances like cetuximab appears feasible with the approach of AFM-IR spectromicroscopy. From the sample preparation point of view the



experiments required 1 μm thick slices of snap frozen TOM models, which are routinely used in histopathology. This avoids high demands on sample preparation as for other label-free spectromicroscopy methods, such as scanning transmission X-ray microscopy.

Cetuximab clearly does not bind to structures in the cell membrane but is taken up into the cells or may even leave the sample during the cultivation of the TOM model and prior to the analysis. The amount of cytosolic cetuximab is low and cetuximab does not penetrate the cell nuclei. The present results substantiate by label-free spectromicroscopy the known limited efficacy of cetuximab. The distribution of cetuximab does not depend crucially on the administration route, but somewhat more cetuximab was found in the systemically treated TOM model. Finally, this label-free detection by AFM-IR can be used for identifying drugs, provided that reliable reference spectra, an untreated reference sample, and spectrally distinct regions are present that allow one to identify the drugs of interest.

Conflicts of interest

There are no conflicts of interest to declare.

Acknowledgements

Financial support by Freie Universität Berlin is gratefully acknowledged. RBR thanks the Freie Universität Berlin for funding of a guest stay in preparation for a Humboldt Research Fellowship for postdoctoral and experienced researchers. ER acknowledges financial support by Deutsche Forschungsgemeinschaft (DFG) (grants: RU 420/12-1 and RU 420/13-1).

References

- 1 L. C. Tsao, J. Force and Z. C. Hartman, *Cancer Res.*, 2021, **81**, 4641–4651.
- 2 J. D. Wolchok, V. Chiarion-Sileni, R. Gonzalez, P. Rutkowski, J. J. Grob, C. L. Cowey, C. D. Lao, J. Wagstaff, D. Schadendorf, P. F. Ferrucci, M. Smylie, R. Dummer, A. Hill, D. Hogg, J. Haanen, M. S. Carlino, O. Bechter, M. Maio, I. Marquez-Rodas, M. Guidoboni, G. McArthur, C. Lebbé, P. A. Ascierto, G. V. Long, J. Cebon, J. Sosman, M. A. Postow, M. K. Callahan, D. Walker, L. Rollin, R. Bhore, F. S. Hodi and J. Larkin, *N. Engl. J. Med.*, 2017, **377**, 1345–1356.
- 3 L. Gronbach, C. Wolff, K. Klinghammer, J. Stellmacher, P. Jurmeister, U. Alexiev, M. Schäfer-Korting, I. Tinhofer, U. Keilholz and C. Zoschke, *Biomaterials*, 2020, **258**, 120277.
- 4 L. Gronbach, P. Jurmeister, M. Schäfer-Korting, U. Keilholz, I. Tinhofer and C. Zoschke, *Front. Bioeng. Biotechnol.*, 2020, **8**, 579896.
- 5 P. Volz, A. Boreham, A. Wolf, T.-Y. Kim, J. Balke, J. Frombach, S. Hadam, Z. Afraz, F. Rancan, U. Blume-Peytavi, A. Vogt and U. Alexiev, *Int. J. Mol. Sci.*, 2015, **16**, 6960–6977.
- 6 R. Brodewolf, P. Volz-Rakebrand, J. Stellmacher, C. Wolff, M. Unbehauen, R. Haag, M. Schäfer-Korting, C. Zoschke and U. Alexiev, *Theranostics*, 2020, **10**, 6322–6336.
- 7 K. Prakash, B. Diederich, R. Heintzmann and L. Schermelleh, *Philos. Trans. R. Soc., A*, 2022, **380**, 20210110.
- 8 X. Ma and F. M. Fernandez, *Mass Spectrom. Rev.*, 2022, **43**, 235–268.
- 9 N. Eladawi, M. Elmogy, M. Ghazal, A. H. Mahmoud, H. Mahmoud, M. T. Alhalabi, A. Aboelfetouh, A. Riad, R. Keynton, S. Schaal and A. El-Baz, in *Diabetes and Fundus OCT*, ed. A. S. El-Baz and J. S. Suri, Elsevier, 2020, pp. 191–221.
- 10 K. Yamamoto, A. Klossek, R. Flesch, T. Ohigashi, E. Fleige, F. Rancan, J. Frombach, A. Vogt, U. Blume-Peytavi, P. Schrade, S. Bachmann, R. Haag, S. Hedtrich, M. Schäfer-Korting, N. Kosugi and E. Rühl, *J. Controlled Release*, 2016, **242**, 64–70.
- 11 G. Germer, T. Ohigashi, H. Yuzawa, N. Kosugi, R. Flesch, F. Rancan, A. Vogt and E. Rühl, *ACS Omega*, 2021, **6**, 12213–12222.
- 12 C. W. Freudiger, W. Min, B. G. Saar, S. Lu, G. R. Holtom, C. W. He, J. C. Tsai, J. X. Kang and X. S. Xie, *Science*, 2008, **322**, 1857–1861.
- 13 A. Klossek, S. Thierbach, F. Rancan, A. Vogt, U. Blume-Peytavi and E. Rühl, *Eur. J. Pharm. Biopharm.*, 2017, **116**, 76–84.
- 14 G. J. Zhang, D. J. Moore, C. R. Flach and R. Mendelsohn, *Anal. Bioanal. Chem.*, 2007, **387**, 1591–1599.
- 15 B. Kästner, C. M. Johnson, P. Hermann, M. Kruskopf, K. Pierz, A. Hoehl, A. Hornemann, G. Ulrich, J. Fehmel, P. Patoka, E. Rühl and G. Ulm, *ACS Omega*, 2018, **3**, 4141–4147.
- 16 F. Keilmann, A. J. Huber and R. Hillenbrand, *J. Infrared, Millimeter, Terahertz Waves*, 2009, **30**, 1255–1268.
- 17 A. Dazzi and C. B. Prater, *Chem. Rev.*, 2017, **117**, 5146–5173.
- 18 F. Lu, M. Jin and M. A. Belkin, *Nat. Photonics*, 2014, **8**, 307–312.
- 19 K. Rajes, K. A. Walker, S. Hadam, F. Zabihi, J. Ibrahim-Bacha, G. Germer, P. Patoka, B. Wassermann, F. Rancan, E. Rühl, A. Vogt and R. Haag, *ACS Biomater. Sci. Eng.*, 2021, **7**, 2485–2495.
- 20 J. G. Rheinwald and M. A. Beckett, *Cancer Res.*, 1981, **41**, 1657–1663.
- 21 A. Barth and C. Zscherp, *Q. Rev. Biophys.*, 2002, **35**, 369–430.
- 22 A. Barth, *Biochim. Biophys. Acta*, 2007, **1767**, 1073–1101.
- 23 J. C. Nash and S. Shlien, *Comput. J.*, 1987, **30**, 268–275.
- 24 X. D. Zhang, R. Balhorn, J. Mazrimas and J. Kirz, *J. Struct. Biol.*, 1996, **116**, 335–344.
- 25 I. N. Koprinarov, A. P. Hitchcock, C. T. McCrory and R. F. Childs, *J. Phys. Chem. B*, 2002, **106**, 5358–5364.



- 26 G. Germer, T. Ohigashi, H. Yuzawa, N. Kosugi, R. Flesch, F. Rancan, A. Vogt and E. Rühl, *J. Electron Spectrosc. Relat. Phenom.*, 2023, **266**, 147343.
- 27 G. Germer, *Linear Combination Modeling*, WaveMetrics Inc., Portland, OR, U.S.A., 5.07th edn, 2023.
- 28 I. S. Dhillon and S. Sra, presented in part at the Proceedings of the 18th International Conference on Neural Information Processing Systems, Vancouver, British Columbia, Canada, 2005.
- 29 H. Tanimoto, H. K. Xu, M. Mizumaki, Y. Seno, J. Uchiwada, R. Yamagami, H. Kumazoe, K. Iwamitsu, Y. Kimura, K. Amezawa, I. Akai and T. Aonishi, *J. Phys. Commun.*, 2021, **5**, 115005.
- 30 A. Z. Samuel, S. Horii, M. Ando and H. Takeyama, *Anal. Chem.*, 2021, **93**, 12139–12146.
- 31 H. Shinzawa, K. Awa, W. Kanematsu and Y. Ozaki, *J. Raman Spectrosc.*, 2009, **40**, 1720–1725.
- 32 J. B. Vermorken, J. Trigo, R. Hitt, P. Koralewski, E. Diaz-Rubio, F. Rolland, R. Knecht, N. Amellal, A. Schueler and J. Baselga, *J. Clin. Oncol.*, 2007, **25**, 2171–2177.
- 33 A. A. Govyadinov, S. Mastel, F. Golmar, A. Chuvilin, P. S. Carney and R. Hillenbrand, *ACS Nano*, 2014, **8**, 6911–6921.
- 34 P. Patoka, G. Ulrich, A. E. Nguyen, L. Bartels, P. A. Dowben, V. Turkowski, T. S. Rahman, P. Hermann, B. Kästner, A. Hoehl, G. Ulm and E. Rühl, *Opt. Express*, 2016, **24**, 1154–1164.
- 35 B. Hauer, A. P. Engelhardt and T. Taubner, *Opt. Express*, 2012, **20**, 13173–13188.
- 36 W. Zhang and Y. Chen, *Opt. Express*, 2020, **28**, 6696–6707.
- 37 A. Karpinska, G. Magiera, K. Kwapiszewska and R. Hołyst, *J. Phys. Chem. Lett.*, 2023, **14**, 1272–1278.
- 38 C. Li, M. Iida, E. F. Dunn, A. J. Ghia and D. L. Wheeler, *Oncogene*, 2009, **28**, 3801–3813.
- 39 Y. Chen, G. H. Liu, L. F. Guo, H. Wang, Y. Fu and Y. Z. Luo, *Int. J. Cancer*, 2015, **136**, 182–194.
- 40 F. S. Ruggeri, B. Mannini, R. Schmid, M. Vendruscolo and T. P. J. Knowles, *Nat. Commun.*, 2020, **11**, 2945.
- 41 J. Waeytens, J. De Meutter, E. Goormaghtigh, A. Dazzi and V. Raussens, *Anal. Chem.*, 2023, **95**, 621–627.
- 42 A. M. Chizhik, D. Ruhlandt, J. Pfaff, N. Karedla, A. I. Chizhik, I. Gregor, R. H. Kehlenbach and J. Enderlein, *ACS Nano*, 2017, **11**, 11839–11846.
- 43 B. Kästner, F. Schmähling, A. Hornemann, G. Ulrich, A. Hoehl, M. Kruskopf, K. Pierz, M. B. Raschke, G. Wübbeler and C. Elster, *Opt. Express*, 2018, **26**, 18115–18124.
- 44 M. Marschall, A. Hornemann, G. Wübbeler, A. Hoehl, E. Rühl, B. Kästner and C. Elster, *Opt. Express*, 2020, **28**, 38762–38772.
- 45 B. Kästner, M. Marschall, A. Hornemann, S. Metzner, P. Patoka, S. Cortes, G. Wübbeler, A. Hoehl, E. Rühl and C. Elster, *Meas. Sci. Technol.*, 2024, **35**, 015403.

